Computers in Biology and Medicine 110 (2019) 66–78

Contents lists available at ScienceDirect

Computers in Biology and Medicine

journal homepage: www.elsevier.com/locate/compbiomed

Slice interpolation of medical images using enhanced fuzzy radial basis function neural networks

Zhen Chao[a], Hee-Joung Kim[a,b,*]

[a] Department of Radiation Convergence Engineering, College of Health Science, Yonsei University, 1Yonseidae-gil, Wonju, Gangwon, 220-710, South Korea
[b] Department of Radiological Science, College of Health Science, Yonsei University, 1Yonseidae-gil, Wonju, Gangwon, 220-710, South Korea

ARTICLE INFO

Keywords:
Missing slice images
Slice interpolation method
Enhanced radial basis function neural network
Hybrid of gravity search algorithm and error backpropagation algorithm

ABSTRACT

Volume data composed of complete slice images play an indispensable role in medical diagnoses. However, system or human factors often lead to the loss of slice images. In recent years, various interpolation algorithms have been proposed to solve these problems. Although these algorithms are effective, the interpolated images have some shortcomings, such as less accurate recovery and missing details. In this study, we propose a new method based on an enhanced fuzzy radial basis function neural network to improve the performance of the interpolation method. The neural network includes an input layer (six input neurons), three hidden layers of neurons, and the output layer (one output neuron), and we propose a patch matching method to select the input variables of the neural network. Accordingly, we use two normal pending images to be interpolated as the input. Final output data is obtained by applying the trained neural network. In examining four groups of medical images, the proposed method outperforms five other methods, achieving the highest similarity image metric (ESSIM) values of 0.96, 0.95, 0.94, and 0.92 and the lowest mean squared difference (MSD) values of 35.5, 41.2, 50.9, and 47.1. In addition, for a whole MRI brain volume data experiment, the average MSD and ESSIM values of the proposed method and other methods are (41.62, 0.95) and (57.13, 0.90), respectively. The results indicate that the proposed method is superior to the other methods.

1. Introduction

In the field of modern medicine, Computed Tomography (CT), Magnetic Resonance Imaging (MRI), and other medical imaging technologies are widely used. The series of complete two-dimensional data obtained by medical imaging systems can be improved to three-dimensional volume data by reconstruction technologies that allow the visual display of human tissues or organs [1,2]. However, even though acquisition time, cost, and human exposure dose can be high, some medical imaging devices continue to be used extensively by necessity, such as 32-row or 64-row spiral CTs. In the three-dimensional volume data obtained by these devices, the spacing between slices is often much larger than that between adjacent pixels in the same image volume. If such volume data are directly reconstructed, the results will contain step-like edges, discontinuous surfaces, interrupted details, and other phenomena. Therefore, these incomplete data have lower diagnostic significance [3–5]. Based on this, in order to obtain high resolution and complete volume data, compensation for missing data has become a popular research direction. Slice interpolation methods represent a powerful tool to compensate for missing slice data, as shown in Fig. 1.

For interpolation algorithms, three well-known methods are linear interpolation, nearest-neighbor interpolation, and cubic interpolation. These methods are directly based on pixel gray levels [5–7]. The advantages of these methods are their simple operation principles, low computational complexity, easy implementation, and wide application. However, they ignore an important factor: that pixel changes are caused by an object's structure. This is particularly true for linear interpolation and nearest-neighbor interpolation, which consider very few adjacent pixels for interpolation processing, and thus many relevant pixels cannot be considered. The consequences are that the interpolation accuracy is very low, the resultant images are blurred, some structural details are lost, visual authenticity is poor, and artifacts may occur [5,8]. Subsequently, other pixel-based methods have been proposed [9–12], and have attempted to apply higher numbers of adjacent pixels to interpolation algorithms. Although some progress has been made, the problems involving artifacts and blurring still exist.

In addition, feature-based methods have been gradually developed. This type of method was first proposed by Baghaie et al. [13], the

* Corresponding author. Department of Radiological Science, College of Health Science, Yonsei University, 1Yonseidae-gil, Wonju, Gangwon, 220-710, South Korea.
E-mail address: hjk1@yonsei.ac.kr (H.-J. Kim).

https://doi.org/10.1016/j.compbiomed.2019.05.013
Received 25 March 2019; Received in revised form 15 May 2019; Accepted 15 May 2019

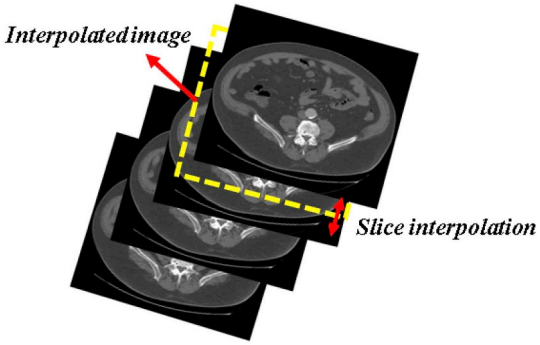

Fig. 1. Slice interpolation demonstration graph based on CT image sequences.

characteristic of which is to extract the input image information and obtain the deformation data corresponding to each pixel of the image to be interpolated. Finally, the pixel values are calculated. Later Penney et al. [14] proposed a method based on non-rigid registration to better find the mapping relationship between slices with similar structural features. In addition, a modified mesh control interpolation method was proposed [15].

Leng et al. [5] developed a multiresolution registration mode as a preprocessing step to improve the interpolation accuracy of the conventional methods. This type of algorithm considers the problem of energy minimization. It is necessary to obtain the deformation field by using appropriate regularization terms and interpolation constraints. The initial value of the deformation iteration is usually rigid or predicted by a ray-like transformation. Based on this, the convergence positions are not ideal if the criterion is not strictly aligned [16,17]. In order not to depend on the initial location of registration, a series of curvature-based registration methods were proposed [17–19]. They avoid the influence of an unreliable preregistration of affine linearity. However, the problem of unsatisfactory effects has not been solved thoroughly for situations where the pending structural differences between consecutive slices are large. Recently, deep learning technology has been widely used to improve image quality or create super-resolution images. Park et al. [20] applied U-net model to CT super-resolution. You et al. [21] proposed the generative adversarial network (GAN)- based method to create CT super-resolution. The multi-scale fusion convolution network (MFCN) was proposed to improve the quality of MR images [22]. These methods made corresponding contributions. However, it needs to be noted that training convolutional neural networks requires big data. If the data is insufficient, the performance of deep learning will be greatly limted.

In this paper, in view of the shortcomings of the above state-of-the-art methods, we propose a new method based on an enhanced Takagi–Sugeno fuzzy radial basis function neural network (EF-RBFNN). The enhanced system includes five layers. The structure ratio of the input layer to the output layer is 6:1. Therefore, based on a particular interpolation data point, six corresponding adjacent normal data points are used as input. The operation mechanism of the entire neural network conforms to the classical T–S fuzzy model [23,24].

The error backpropagation algorithm (EBPA) is one of the earliest training methods for neural networks, but its effectiveness depends highly on the network parameters [25]. In heuristic optimization methods, the ability of the gravitational search algorithm (GSA) to find the best solution has been proven many times [26–29]. However, owing to the complexity of the algorithm, the corresponding search speed is relatively slow [30,31]. We previously proposed a hybrid of the GSA and EBPA and successfully applied it to the training of feedforward neural networks [32]. In addition, to construct a fitness function, we applied a curvature-based method which can select ideal output data.

In summary, for specific processing pixel, we substitute six input pixels. In turn, we can obtain the initial data aimed at producing an entire interpolated image. A certain number of training cycles is subsequently applied to continuously optimize the neural network. Finally, we can obtain the optimal output through the updated neural network. To validate the performance of the proposed neural network, we compare its performance to the classic linear interpolation method and the state-of-the-art multiresolution method. The final experimental results verify that the proposed method outperforms these methods.

2. Materials and methods

2.1. Curvature-based model

The curvature-based model uses nonparametric image registration. It does not need to extract specific feature points, nor does it need to specify parameters to conduct a model transformation [33]. This model is commonly expressed as

$$E(\mu) = D[R, T; \mu] + \alpha S \quad (1)$$

where R is a reference image, T is a floating image. μ is the deformation field between these images, and D is a similarity measure function. The regularization term S represents the smoothing speed function, and α is a smoothing coefficient. The significance of this equation is that we need to find the value of μ that minimizes the energy function E. Because this model is a single-direction model, Baghaie et al. [16] proposed an optimized curvature-based model to make it suitable for processing two images and improve its performance, as follows:

$$E(\mu) = \frac{1}{2}\int_{\Omega} (R_1(x - r_1\mu(x)) - R_2(x + r_2\mu(x)))^2 dx + \frac{\alpha}{2}\sum_{l=1}^{2}\int_{\Omega} (\Delta\mu_l)^2 dx \quad (2)$$

From Eq. (2), with the plus sign as the dividing mark, the first half of the expression is actually a similarity measure function or distance measure function. R_1 and R_2 are pending images, $r_1 = d_1/(d_1 + d_2)$, $r_2 = 1 - r_1$, and d_1 and d_2 represent the distance between two pending images and two interpolated images, respectively. For the smoothness function S (the second half of Eq. (2)), Δ represents the curvature operator. The dimension is 1. Accordingly, the function S computes the summation over two dimensions of the image.

Based on this model, the energy function E is minimized to obtain μ by applying Gateaux derivatives of the similarity measure and smoothness term as follows:

$$f(x, \mu(x)) + \alpha\Delta^2\mu(x) = 0, x \in \Omega \quad (3)$$

$$f(x, \mu(x)) = (R_2(x + r_2\mu) - R_1(x - r_1\mu))\cdot(\nabla R_1(x - r_1\mu) + \nabla R_2(x + r_2\mu)) \quad (4)$$

Subsequently, after a series of formulaic operations, the final deformation field μ can be obtained. Specific operational details can be found in Refs. [16,33].

In Ref. [16], the interpolated images can be obtained by averaging the two transformed input images as follows:

$$Resultant\ image = \frac{R_2(x + r_2\mu_{final}) + R_1(x - r_1\mu_{final})}{2} \quad (5)$$

However, in our experiments, this simple average interpolation method is more effective when there is little structural difference between images. When there is a large structural difference between images, the performance of the basic method is not ideal. Therefore, we propose a new interpolation method based on a Takagi–Sugeno fuzzy radial basis function neural network (Fuzzy-RBFNN).

2.2. Takagi–Sugeno fuzzy model and radial basis function neural network

The well-known Takagi–Sugeno (T–S) fuzzy model was first proposed in Ref. [23]. It adopts the “If-Then” rule. The “Then” part is an exact function that is usually a variable polynomial. Accordingly, the

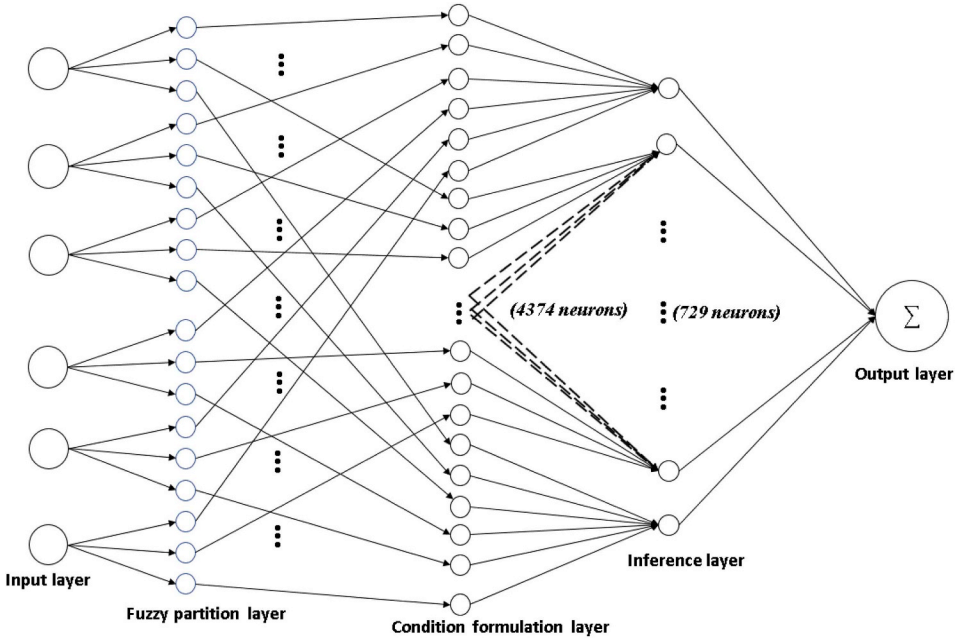

Fig. 2. Structure of enhanced Fuzzy-RBFNN system.

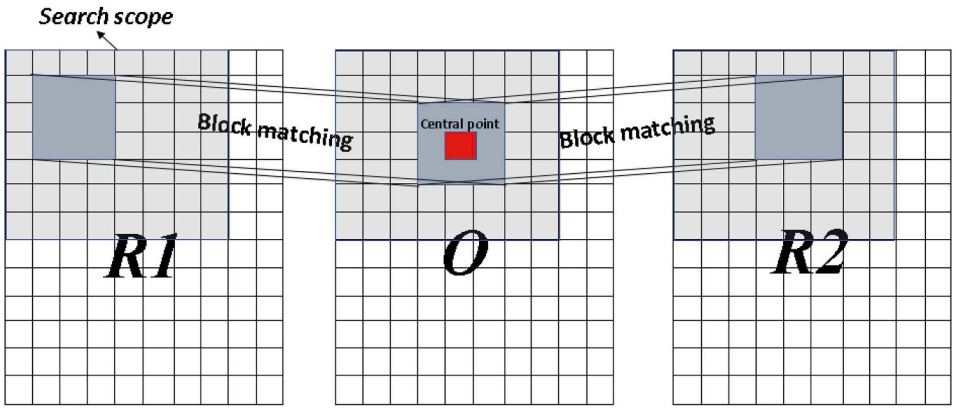

Fig. 3. Window matching example.

T–S model can generate a high number of complex nonlinear functions with a small number of fuzzy rules that can effectively reduce the total number of fuzzy rules used to describe multivariable systems. Therefore, it is advantageous in the analysis and synthesis of complicated nonlinear systems [34]. The T–S fuzzy rule is commonly expressed as follows:

$$R^l: \textit{If } x_1 \textit{ is } K_1^l,\ x_2 \textit{ is } K_2^l,\ \ldots,\ x_n \textit{ is } K_n^l,\ \textit{Then } y^l = \sum_1^n a_i^l x_i^l + b^l \quad i = 1, 2, \ldots, n \tag{6}$$

where l = 1, 2, …, m, and m represents the number of fuzzy rules; [x_1, x_2, …, x_n] is the set of input variables; and [K_1, K_2, …, K_n] represents fuzzy sets of the corresponding input variables. A fuzzy set K_i can be further divided into several fuzzy subsets K_{ij}, (j = 1, 2, …, o), where o is the number of fuzzy subsets. A fuzzy subset represents a membership function, and is commonly defined by a Gaussian function as follows:

$$K_{ij}^l(x_i) = exp\left(-\frac{1}{2}\left(\frac{x_i - c_{ij}^l}{\sigma_{ij}^l}\right)^2\right) \tag{7}$$

where c and σ represent the center and width of the Gaussian function, respectively. After performing all rule operations, the final output of the fuzzy model can be expressed as follows:

$$y = \frac{\sum_{l=1}^m v^l y^l}{\sum_{l=1}^m v^l} \tag{8}$$

where v^l represents the weight of the lth rule, and is defined as follows:

$$v^l = \prod_{i=1}^n K_i^l(x_i) \tag{9}$$

A radial basis function (RBF) network is a forward network based on function approximation theory. The basic idea behind an RBF neural network is to use the RBF as the “base” of the hidden units to form the hidden layer space so that input vectors can be mapped directly to the hidden space without connection weights. When the central point of the RBF is determined, the mapping relationship is determined. The mapping from the hidden layer space to the output space is linear, that is, the network output is the weighted sum of the output of the hidden units [35,36]. Accordingly, RBF neural networks and fuzzy systems are structurally equivalent. Their combination is the key technology in realizing an intelligent simulation, which can be adapted to more complicated problems or fields and has stronger intelligent characteristics [37].

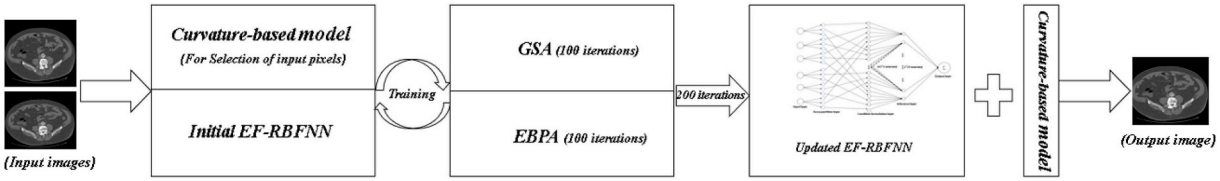

Fig. 4. Flowchart of proposed model based on EF-RBFNN.

Table 1
Parameters for the three groups of data.

data	size	Selected sequence	Slice distance
MRI brain data	512 × 512 × 352	173rd 174th 175th	1.5 mm
		126th 128th 130th	3 mm
CT chest data	512 × 512 × 200	158th 160th 162nd	4 mm
CT brain data	256 × 256 × 108	74rd 76th 78th	4 mm

Underlined items represent interpolated slices.

2.3. Proposed enhanced fuzzy radial basis function neural network

Accordingly, we propose the enhanced fuzzy radial basis function neural network (EF-RBFNN) with a "6-18-4374-729-1" structure. That is, the EF-RBFNN is divided into five layers: input, fuzzy partition, condition formulation, inference, and output. The number of neurons in the respective layers is 6, 18, 4374, 729, and 1, as shwon in Fig. 2. In the input layer, the six neurons represent six input variables. In the fuzzy partition layer, each input variable is divided into three fuzzy subsets. The condition formulation layer and inference layer are collectively called the rule-making layer. Every six neurons of the condition formulation layer are mapped to one neuron of the inference layer. Finally, we can determine the output variable in the output layer according to Eq. (8).

2.3.1. Selection of input variables of neural networks

For selecting of input variables of neural networks, we propose a hybrid of patch matching and pixel similarity method, as follow:(see

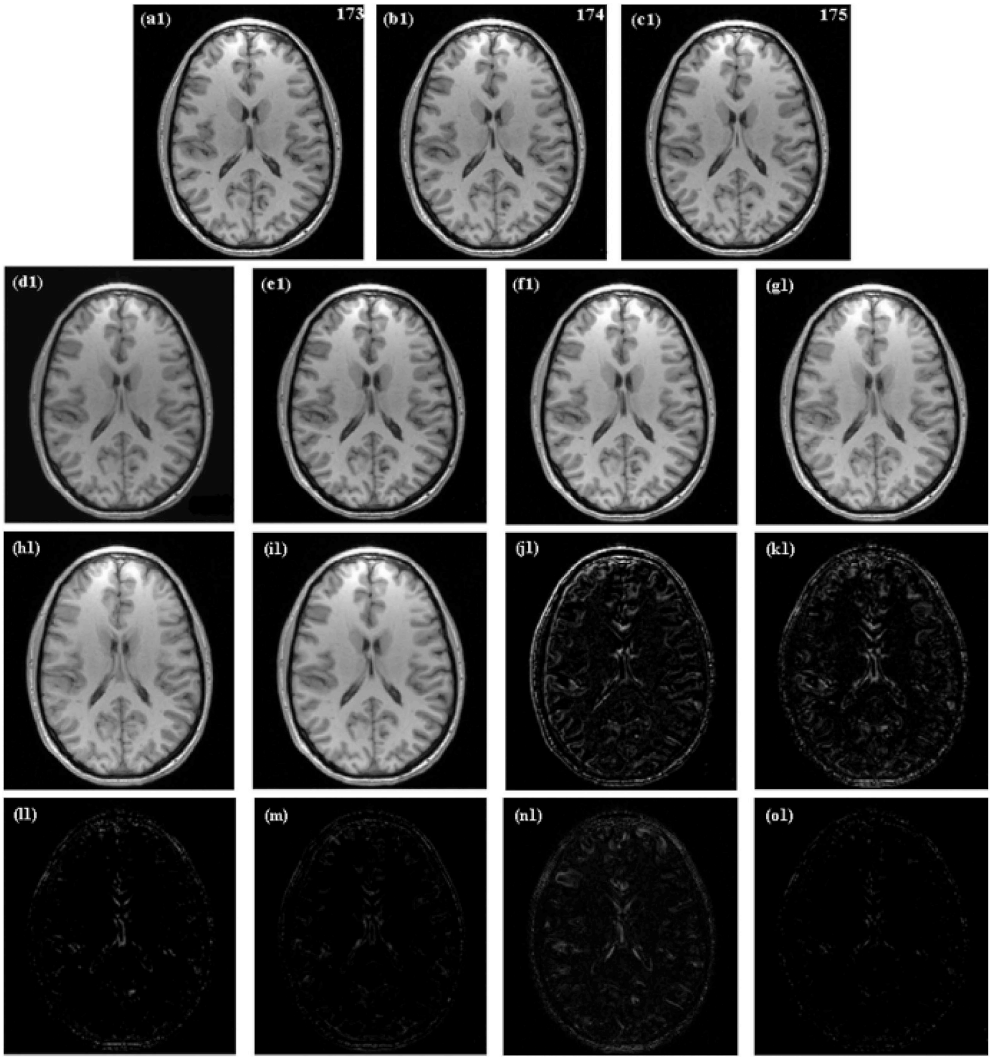

Fig. 5. Performance comparison for brain MRI data 1: (a1–c1) 173rd, 174th, and 175th slice images, where a1 and c1 are pending images and b1 is the reference image; (d1–i1) are interpolated images using the linear interpolation method, multiresolution method, curvature-based method, high order method, proposed method with RBF model, and proposed method, respectively; (j1–o1) are difference images corresponding to (d1–i1).

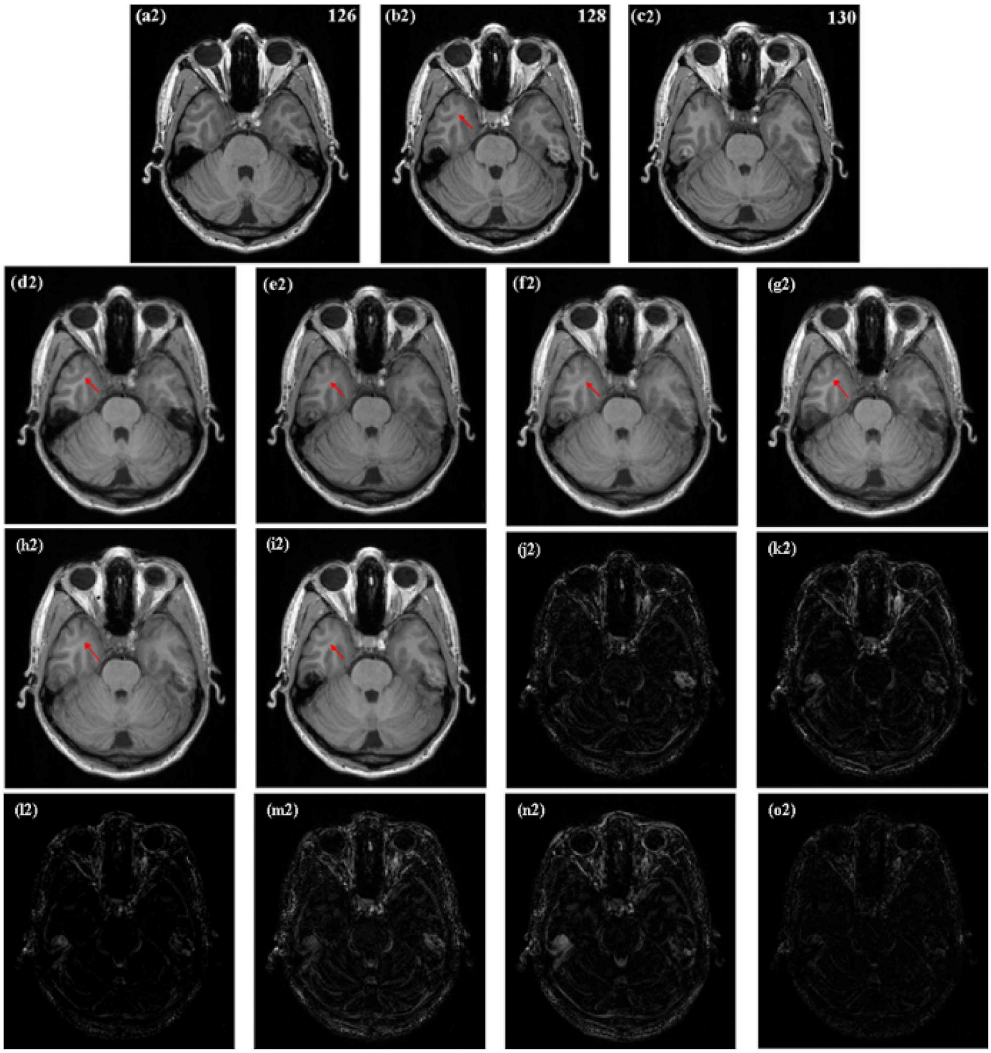

Fig. 6. Performance comparison for brain MRI data 2: (a2–c2) 126th, 128th, and 130th slice images, where a2 and c2 are pending images and b2 is the reference image; (d2–i2) are interpolated images using the linear interpolation method, multiresolution method, curvature-based method, high order method, proposed method with RBF model, and proposed method, respectively; (j2–o2) are difference images corresponding to (d2–i2).

Algorithm 1)

Algorithm. *: The hybrid of patch matching and pixel similarity*

Require: R_1 and R_2 (two pending images).

Require: R_1 ($x - r_1\mu_{final}$) and R_2 ($x + r_2\mu_{final}$) (two registered images based on R_1 and R_2 by applying the curvature-based model.

Require: O (the resultant image obtained by Eq, (5).

Step1: Select a certain pixel of image O. With this pixel as the center, its neighborhood (in a 3 × 3 window) is delineated.

Step2: Based on this neighborhood window, we find the matching windows in the images R_1 and R_2 by the Sum of Squared Differences (SSD) per Eq. (10). The search scope is 25 × 25. To make this easier to understand, we provide a simulated diagram, as shown in Fig. 3

$$SSD = \sum_{i=1}^{M}\sum_{j=1}^{N}[R(i,j) - O(i,j)]^2 \quad M(N) = 3 \tag{10}$$

Step3: Calculate the gradient azimuth of each pixel of the two matching windows and the central pixel. The calculation of the gradient azimuth is accomplished by applying Eqs. (2)–(7) of [38].

Step4: Apply Eq. (11) to find pixels that are similar to the center point.

$$Similar\ pixel = \omega(j,k) \times |A_i(j,k) - B| \qquad i = 1,\ 2 \tag{11}$$

$$(j,k) = \frac{|\Delta_{A_i}(j,k) - \Delta_B|}{\pi} \qquad |\Delta_{A_i}(j,k) - \Delta_B| = 0 \rightarrow \pi \tag{12}$$

where A_i(j, k) is the pixel value at (j, k) of window A, and j, k ∈ {1, 2, 3}; B is the pixel value of the central point; and Δ is the gradient azimuth at (j, k). It must be noted that if the difference in angle is larger than π, we need to subtract the difference by 2π to obtain the correct azimuth difference.

Step5: select three pixels each from R_1 and R_2 that have the least differences with the center point. That is, these six pixels are treated as input variables of the neural network.

2.3.2. Further explanation of neural network based on slice interpolation

Based on a certain pixel of the registered image, six pixels (3-3) are selected from the two pending images. Each pixel is divided into three fuzzy subsets, which are expressed by Eq. (7). Subsequently, by using the condition formulation layer and the inference layer, where the condition formulation layer represents the conditions of rules and the inference layer represents the result of rules, an overall rule is established based on the combination of the six fuzzy subsets from the corresponding fuzzy sets. That is, six conditions determine a rule. By random allocation, there are 4374 (729 × 6) conditions that define all corresponding rules. Namely, there are 4374 neurons in the condition

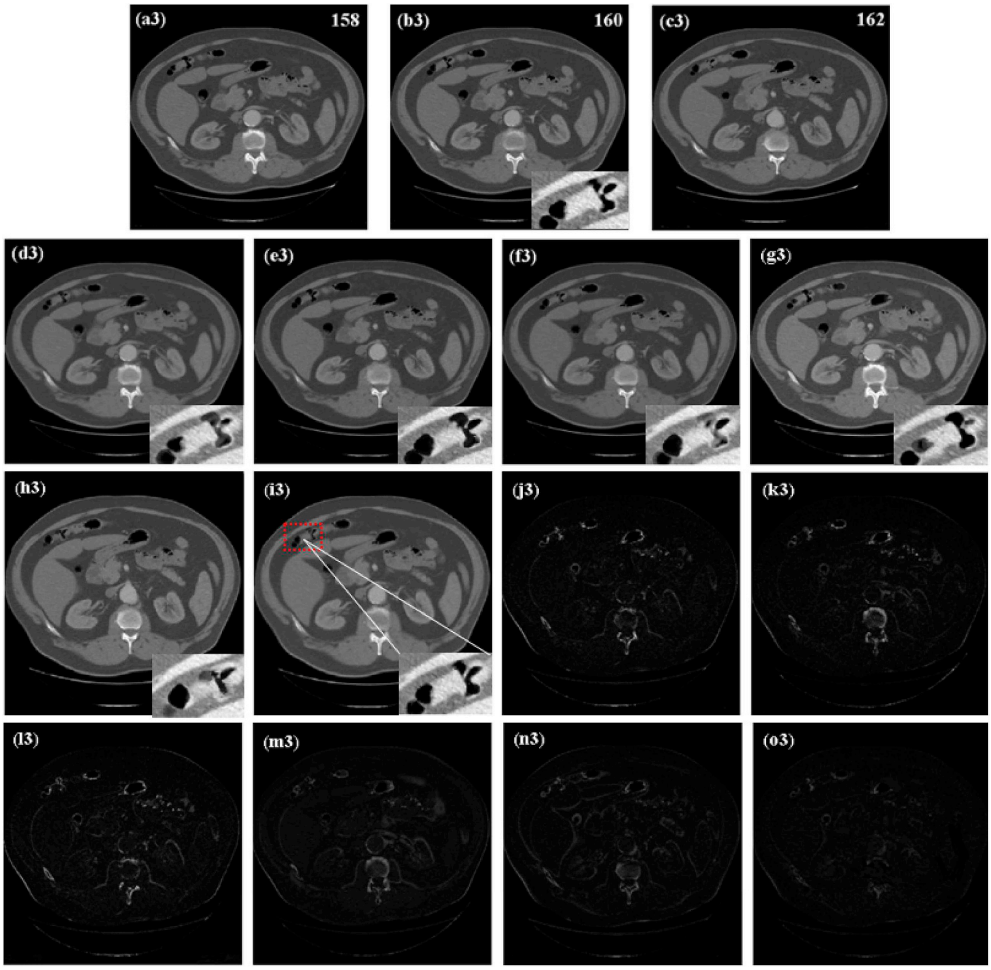

Fig. 7. Performance comparison for chest CT data: (a3–c3) 158th, 160th, and 162nd slice images, where a3 and c3 are pending images and b3 is the reference image; (d3–i3) are interpolated images using the linear interpolation method, multiresolution method, curvature-based method, high order method, proposed method with RBF model, and proposed method, respectively; (j3–o3) are difference images corresponding to (d3–i3).

formulation layer, and 729 rules (neurons) are represented in the inference layer. Finally, the output pixel can be obtained from Eq. (8). Successively, by processing the entire registered image, we obtain all of the output data needed to interpolate an image.

2.4. Training of enhanced fuzzy radial basis function neural network

In the initial stage, the parameters of the neural network are set randomly or empirically. Thus, we need to continuously optimize the neural network through training. In our previous study, we successfully used a hybrid combination of the gravitational search algorithm (GSA) and error backpropagation algorithm (EBPA) to train a Fuzzy-RBFNN for medical image fusion [32]. In this study, we also apply this training method to an EF-RBFNN. The overall idea is to consider the shortcomings of both algorithms by implementing the GSA algorithm first, and then the EBPA algorithm.

The structural characteristics of the neural network require that the parameters c, σ, a, and b be trained into the EF-RBFNN. Based on this, we selected 50 agents as the initial population of the GSA, which included 5139 values (dimensions), as follows:

$$X_i = (X_i^1, \cdots, X_i^{18}, X_i^{19}, \cdots, X_i^{36}, X_i^{37}, \cdots, X_i^{4410}, X_i^{4411}, \cdots, X_i^{5139}) \quad 13$$

where X^1–X^{18} and X^{19}–X^{36} represent the centers c and widths σ of 18 Gaussian functions and X^{37}–X^{4410} and X^{4411}–X^{5139} represent the coefficients a and b of all rules. i = 1, 2, …, 50. Using the initial EF-RBFNN (which is not trained), we obtain 50 groups of output data that can be named as actual output data A. In addition, the velocity vector V of the agents is also defined and has the same structure as X. The mass is calculated by assuming that the gravitational mass and inertial mass (we name them M) are equal. The mass M of each agent is then defined as follows:

$$\mathrm{m}_i(t) = \frac{fit_i(t) - worst(t)}{best(t) - worst(t)} \quad 14$$

$$M_i(t) = \frac{m_i(t)}{\sum_{j=1}^{50} m_j(t)} \quad 15$$

where $\mathrm{fit_i}$ represents the fitness function of the ith agent, as given by Eq. (14). Best and worst represent the best fitness function values and the worst fitness function values for all agents, as defined by Eqs. (15) and (16), where t represents the iteration time.

$$\mathrm{fit_i} = \frac{\sum_{k=1}^{\mathrm{N}} (A_i^k - B^k)^2}{N} \quad 16$$

In Eq. (14), N is the number of pixels and B is the ideal output data obtained using the curvature-based method [16].

$$best(t) = \min_{i \in \{1,2,\cdots,50\}} fit_i(t) \quad 17$$

$$worst(t) = \max_{i \in \{1,2,\cdots,50\}} fit_i(t) \quad 18$$

Next, we need to calculate the resultant force F and acceleration which is based on Newton's Second Law. Finally, the velocity and

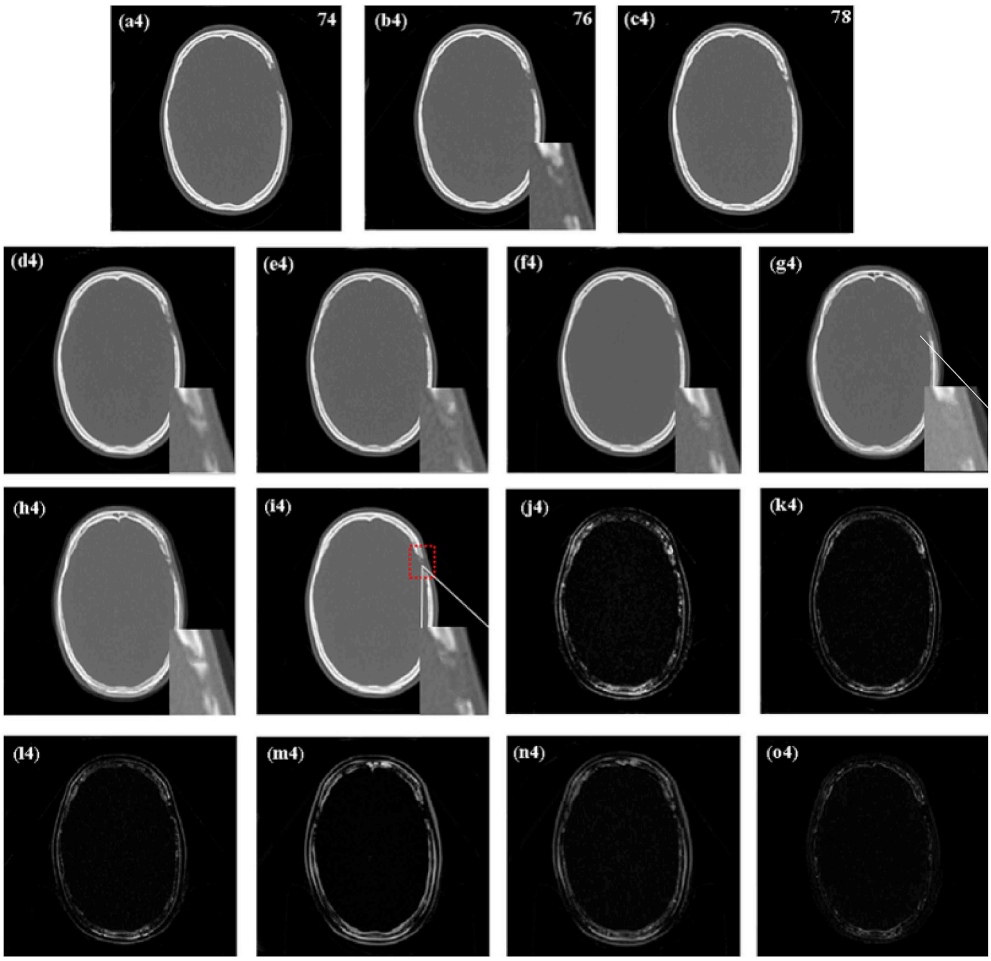

Fig. 8. Performance comparison for brain CT data: (a4–c4) 74th, 76th, and 78th slice images, where a4 and c4 are pending images and b4 is the reference image; (d4–i4) are interpolated images using the linear interpolation method, multiresolution method, curvature-based method, high order method, proposed method with RBF model, and proposed method, respectively; (j4–o4) are difference images corresponding to (d4–i4).

position of agents are updated. The detailed calculation processing of this part can be referred to Ref. [26].

Each agent (representing a set of parameters of EF-RBFNN) was updated by performing 100 iterations. Then, the optimal agent that can be used as the initial parameters of EBPA is determined. EBPA is one of the earliest training methods used, and details of its operation mechanism can be found in Ref. [39]. The algorithm will not be discussed here. It should be noted that the error function required by EBPA is the fitness function in the GSA. Once again, by running 100 iterations on the EBPA, we obtained the final optimal coefficients. Finally, by updating the neural network and curvature-based model, we obtain the final output data, namely, the resultant images. A flowchart of the proposed model is shown in Fig. 4.

2.5. Materials and data analysis

In this paper, we selected three real medical volumetric data items for the experiment: MRI brain data with a $512 \times 512 \times 352$ size, CT chest data with a $512 \times 512 \times 200$ size, and CT brain data with a $256 \times 256 \times 108$ size [40]. For the MRI brain data, we first selected the 173rd and 175th slices to be interpolated. Subsequently, in order to increase the difference in the processed image, the 126th and 130th slices were interpolated. To further demonstrate the clinical significance, the CT chest data of multiple tumors and CT brain data containing various skull defects were included. For the chest data, the 158th and 162nd slices were selected as two pending images, and we applied the 74th and 78th slices in our experiments. In short, the sequence selection principle we adopted was at intervals of one slice or at intervals of three slices in respective volume data. Detailed parameters are listed in Table 1.

To better validate the performance of the proposed method, we also implemented the conventional linear interpolation method and three state-of-the-art methods: the multiresolution method [5], the curvature-based method [16], and the high order method [19] to be compared to the proposed method with RBF model (we select the number of input neurons as six, select the Gaussian function as the activation function, and train the NN by the GSA and EBPA hybrid). In addition, the edge strength similarity image metric (ESSIM) [41] and mean squared difference (MSD) were adopted to provide an objective evaluation.

3. Results

For MRI brain data 1, the 174th slice image was interpolated by two images of the 173rd and 175th slices, as shown in Fig. 5. Subsequently, we selected the 126th and 130th slices to obtain the 128th slice image based on MRI brain data 2, as shown in Fig. 6. For two CT data items with lesions present, Fig. 7 shows that the 160th slice of the CT brain volumetric data was processed based on the 158th and 162nd slices. Finally, we applied the 74th and 78th slices of the CT data displaying skull defects to obtain the 76th slice image, as shown in Fig. 8. In these figures, (a) and (c) represent two images to be interpolated, and (b) is the reference image. Images (d–i) are the interpolated images acquired via the linear interpolation method, the resultant images after applying the state-of-the-art multiresolution method, curvature-based method,

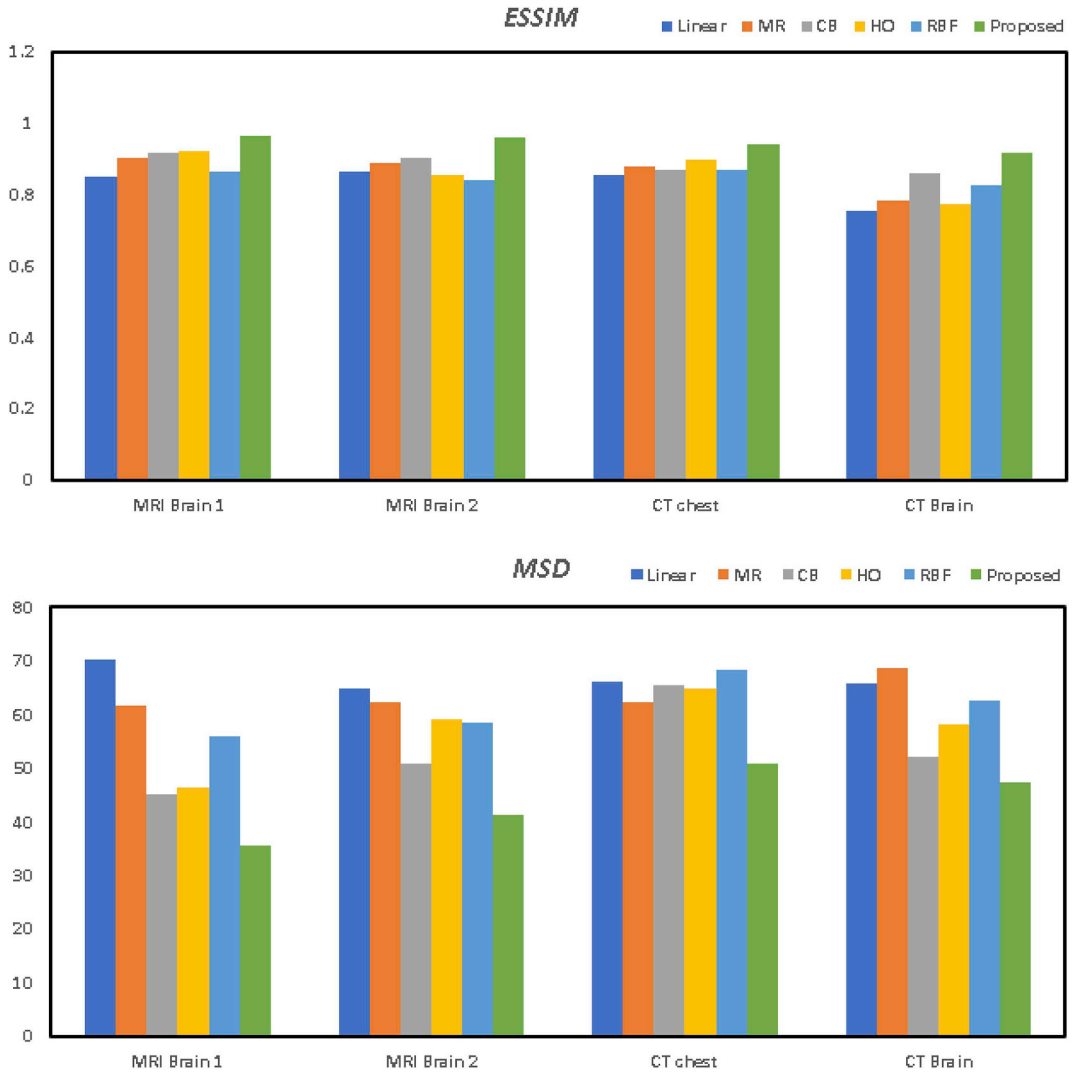

Fig. 9. ESSIM and MSD values for four groups of image data obtained using six different methods.

Table 2
ESSIM performance of three proposed methods based on CT chest data: (b) proposed method, (c) proposed method based on NN with two input neurons, and (d) proposed method based on NN with four input neurons.

CT chest data	(b)	(c)	(d)
ESSIM	**0.94**	0.86	0.87

high order method, the proposed method with RBF model, and the proposed method, respectively.

Indices 1–4 represent the MRI brain data 1 and 2, CT chest data, and CT brain data, respectively. The respective difference images based on the interpolated images and reference image are shown in (j-o) of Figs. 5–8 in order to clearly observe the performance of each method. In addition, in Figs. 7 and 8, we selected a region of interest (ROI) for magnification to more accurately observe the tumors and skull defects, as indicated by the red borders in i3 and i4. The respective ROI images are shown in the lower right corners of the corresponding images.

To analyze the interpolated images more authoritatively and objectively, ESSIM and MSD were applied, as shown in Fig. 9, where Linear, MR, CB, HO, RBF, and proposed are abbreviations for the linear interpolation method, multiresolution method, curvature-based method, high order method, proposed method with RBF, and proposed method, respectively. The lower the value of MSD is, the smaller the deviation between the resultant image and the reference image, indicating better performance. The closer the ESSIM value is to 1, the higher the similarity is between the resultant image and the reference image. Accordingly, for both the MSD and ESSIM indices, the values obtained using the proposed method significantly outperformed those of the five other methods.

4. Discussion

We first discuss the performance of the linear interpolation method and three state-of-the-art methods. Observing MRI brain data 1, as shown in Fig. 5(d–g), the performance of the linear interpolation method was the worst. Differences in the brain circuitry are easily visible compared with the reference image. Especially in the thalamus, the black interspace in the middle of the resultant image is significantly smaller than that in the reference thalamic area. Moreover, the boundaries of the entire structure become blurred, as shown in Fig. 5(b) and (d).

In contrast, the performances of the three state-of-the-art methods (the multiresolution method, the curvature-based method, and the high-order method) are shown in Fig. 5(e–g), respectively. The problems involving structural differences were slightly improved compared to Fig. 5(b). However, after careful observation, the interpolation effects of the thalamus are not suitable because the structural sizes are slightly larger than the size of the structure in the reference image.

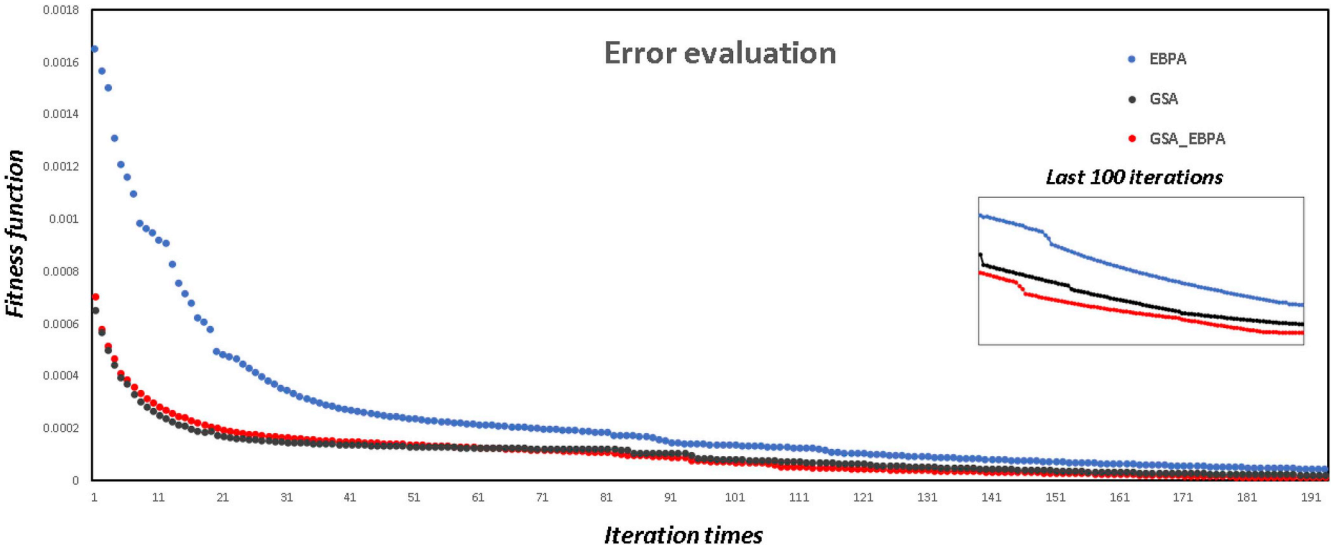

Fig. 10. Convergence performance of three training methods based on MRI brain data 1.

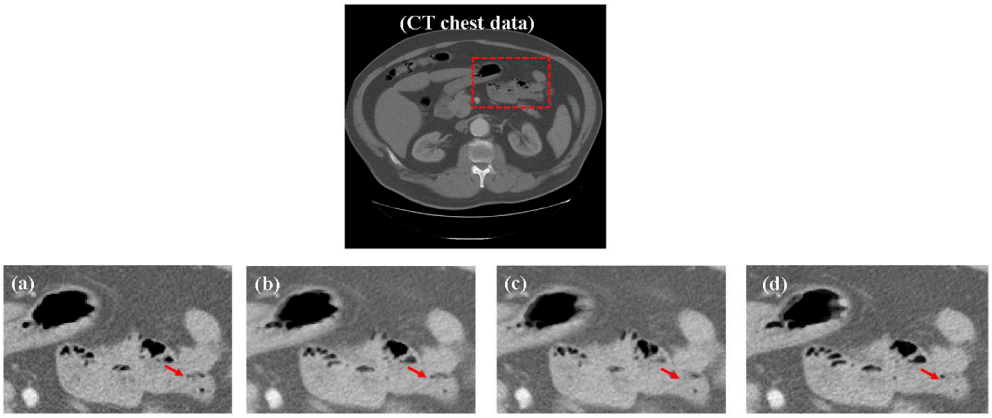

Fig. 11. Correction performance based on CT chest data: (a) reference image, (b) proposed method, (c) proposed method based on NN with two input neurons, and (d) proposed method based on NN with four input neurons.

Next, we increased the interval between the two pending images of MRI brain data 2 to three slices. Therefore, the structural differences in the brain circuits are more obvious between the interpolated images and the reference image when applying the four methods, as shown in Fig. 6(b) and (d–g). Various structural differences are indicated by red arrows. Furthermore, because slice interpolation technology can be more effectively applied to help doctors in the diagnosis of diseases, we implemented two CT data items displaying chest lesions. For the multinodular CT chest data, when directly observing the ROI sections at the lower right corners of Fig. 7(d–g), the reconstruction performance of the tumor shape achieved by the four methods is unsatisfactory compared to the reference tumor shape of Fig. 7(b).

Regarding image blurring, the performance of the linear interpolation algorithm is the most unsatisfactory. The case of a skull defect presented by CT brain scan data is shown in Fig. 8. For slice interpolation, it is a challenging task to reconstruct the details of the skull defects. The performances of the linear interpolation method, the multiresolution method, and the high order method are poor. The phenomena involving loss and distortion of details are obvious. Although the performance of the curvature-based method slightly outperforms that of the three other methods, the loss and distortion phenomena are not improved significantly when the results are compared to the reference image, as shown by the ROIs of Fig. 8(b) and (d–g). All of the problems are better presented in the difference images, as shown in Figs. 5–8(j–m).

As a classic interpolation algorithm, the linear interpolation algorithm has advantages such as fast computation and low budget. However, its simplicity, involving few pixels, easily leads directly to the distortion of image details and blurring of borders [5,42]. The multiresolution method is a combination of the non-rigid registration method and the interpolation method. Its innovation lies in constructing two continuous and regular maps for multiresolution domains. However, this method highly depends on the similarities of anatomical structures. In other words, the appropriate transformation map depends on the initial registration position. Therefore, its use is limited [16]. The curvature-based method is discussed in detail in Section 2.1 of this paper. Correspondences between the two pending images can be found very accurately by the curvature-based model. However, the final interpolation method does not consider the influence of neighboring pixels. The high order method was developed as an extension to the curvature-based method. The point correspondences are first found between pending slices through the curvature-based model. Then, in order to avoid the kink phenomenon, a spline interpolation method is used to smooth out the detail loss caused by the kink phenomenon. There are two possible reasons for poor performance. First, if the number of images to be interpolated is small, the probability of the kink phenomenon will be very large. Second, the problem of over-smoothing is not well considered. Although the performances of the two registration-based algorithms are better than that of the linear interpolation, the results they produce are not ideal in our experiments.

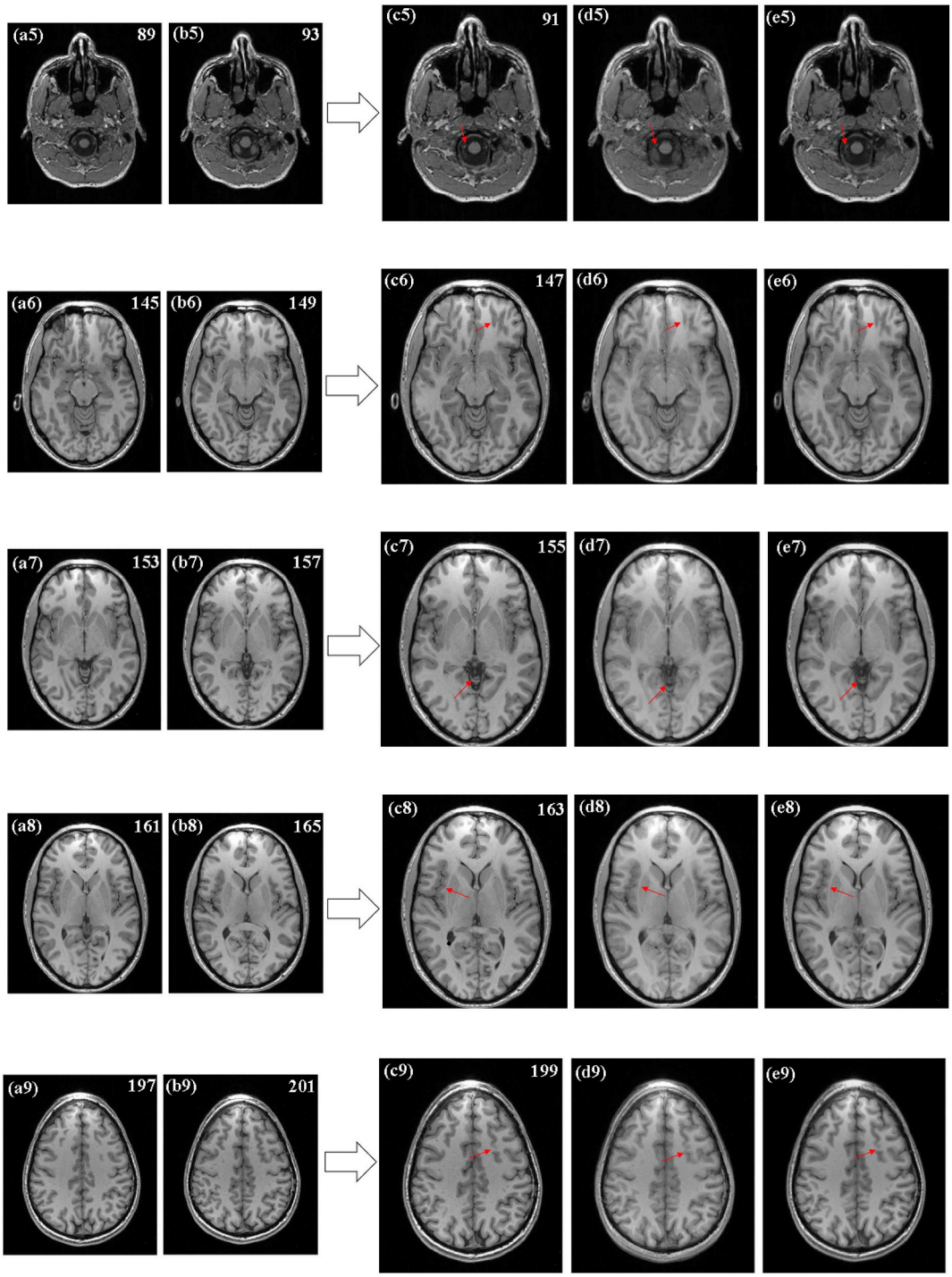

Fig. 12. Performance comparison for partial brain CT volume data: (a–b) pending slice images; (c) reference images, (d) interpolated images using the curvature-based method, and (e) using the proposed method, respectively. The (5–9) labels represent five sets of slices — the 89th, 91st, 93rd; the 145th, 147th, 149th; the 153rd, 155th, 157th; the 161th, 163rd, 165th; and the 197th, 199th, 201th slices, respectively for five interpolations using the proposed and curvature-based methods.

Table 3
Average ESSIM, average MSD, and time cost performance of the proposed method and curvature-based method based on CT brain volume data.

CT brain volume data	Proposed	Curvature-based
Average ESSIM	**0.95**	0.90
Average MSD	**41.62**	57.13
Time cost per data(s)	350.63	**76.49**

Therefore, in order to more effectively implement slice interpolation, we proposed a new method based on the targeted enhanced Fuzzy-RBFNN system. According to the logical relationship of the gray values between the morphological and anatomical structures of the pending images, neural networks with a "6-18-4374-729-1" structure were applied through repeated experiments. Next, we obtained the updated neural network system after a sufficient number of iterations through the GSA and EBPA hybrid. Finally, we obtained the interpolated images by using the optimized EF-RBFNN. The results of the proposed method

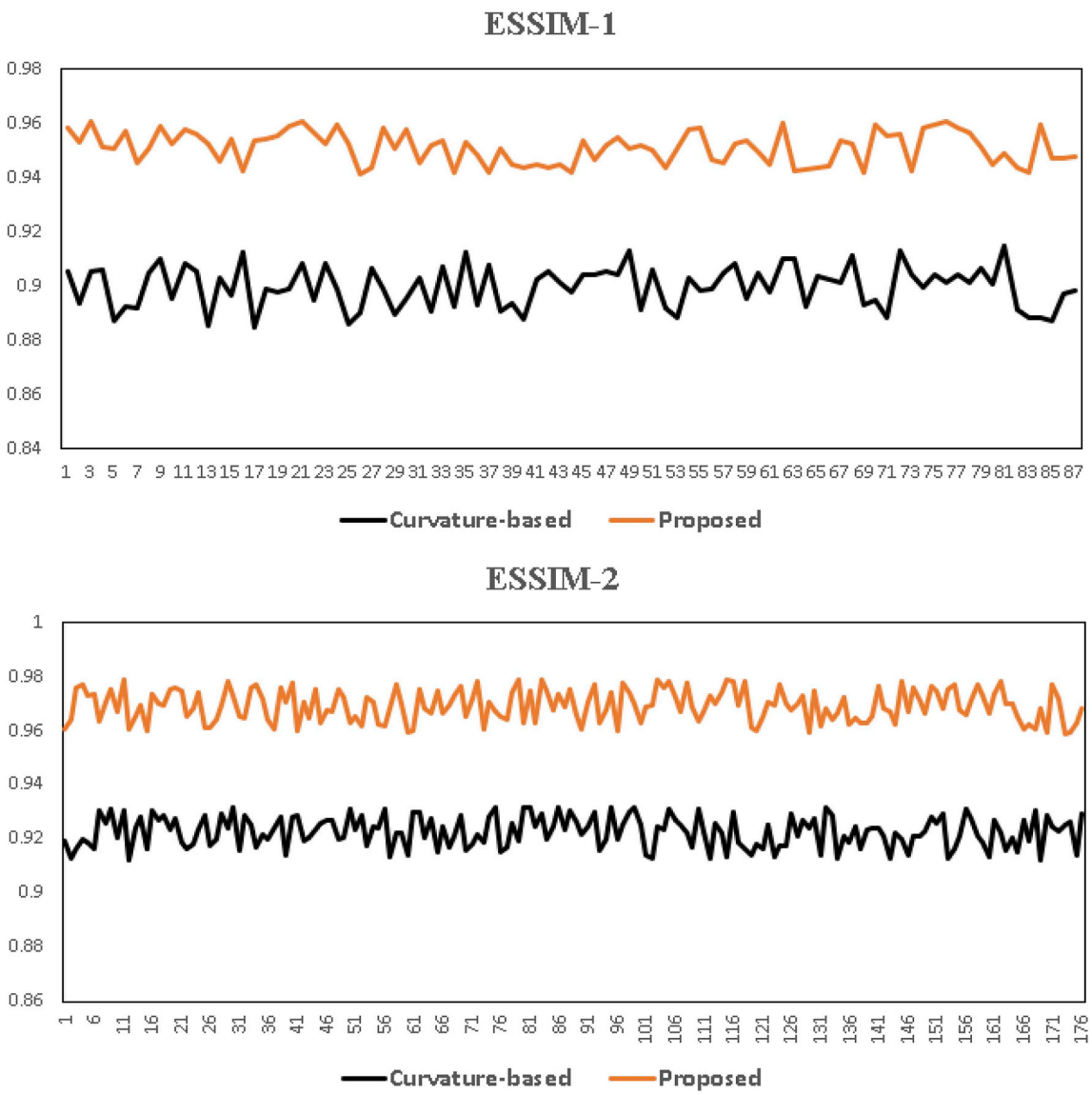

Fig. 13. The sensitivity analysis of ESSIM of the proposed method and curvature-based method based on CT brain volume data. The acquisition mode of ESSIM-1 is every three slices. The acquisition mode of ESSIM-2 is every other slice.

are shown in Figs. 5–8(i) and (o).

For two MRI brain data items, the performance of the proposed method is obviously better when reconstructing changeable brain circuitry and the thalamus. The differences compared to the reference images are also minimal, as shown in Figs. 5 and 6(b) and (d–i). For the CT chest data and CT brain data, the tumor and defective skull morphological structures that were reconstructed by the proposed method were also the closest to the reference image, and retained the structural details and resolution to a greater extent, as shown in Figs. 7 and 8(b) and (d–i). The superiority of the proposed method is also reflected by the objective analysis, achieving the highest ESSIM values and lowest MSD values based on the four experimental data scans.

Now, we further explain the contributions of this paper. The primary contribution is to propose the enhanced Fuzzy-RBF neural network, which is suitable for the slice interpolation of medical images. Compared with our previous studies on neural networks [30], we further update and strengthen the structure of the neural network. The input variables are selected by locating the corresponding pixel points in two images with different structures. Accordingly, we first applied the state-of-the-art curvature-based model to obtain the datum image that connects the two pending images. Then, we apply a patch matching-pixel similarity method using the classic SSD operator, which is widely used in image recognition and matching problems [43,44].

We adopted the SSD to find a matching patch. The sizes of the moving window and searching scale were empirically selected. We needed to find similar pixels in the patch to apply the method successfully. The authors in Ref. [45] applied the root-mean-square deviation, which is based on the pixel value difference, to find similar pixels. However, because we needed to find similar pixels in two small windows that match, we synchronously considered the difference in pixel direction and gray value to find similar pixels instead. For a given number of similar pixels, we conducted three groups of experiments. As alternatives to the proposed method using six pixels, one experiment used two pixels, that is, a single pixel was selected in each of the two matching blocks. The third experiment used four pixels, that is, two pixels were selected in each of the two matching blocks.

The performances based on the CT chest data are shown in Fig. 11(b–d). Fig. 11(b) was obtained by the proposed method with six pixels, and obviously outperforms Fig. 11(c) and (d), which were obtained by the proposed method with two and four pixels, respectively. As the red arrows indicate, some details were lost using the proposed method with two or four pixels, indicating that a minimum of six pixels

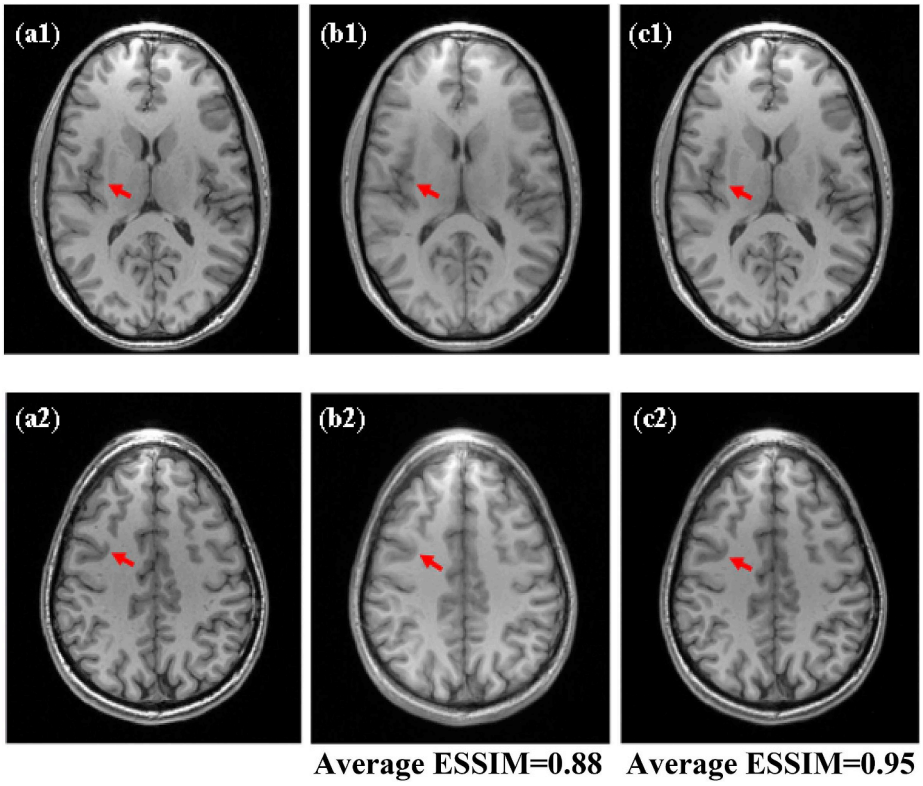

Fig. 14. Performance comparison of U-net and proposed method: (a–c) reference images, resultant images using the U-net method, using the proposed method, respectively. The (1–2) labels represent 171st and 199th slices. Partial differences are marked by red arrows in their respective images. The bottom value represents the ESSIM values of the corresponding methods.

was required to achieve acceptable performance. The performance of the proposed method with six pixels was also better than the two variations based on ESSIM, as shown in Table 2. Therefore, we selected six variables based on empirical analyses as the input for the NN. We will evaluate whether additional pixels provide significant benefit in future work. Calculating the computational cost is also a problem we must consider.

In addition, we succeeded in applying a GSA and EBPA hybrid combination to train the proposed NN. Although this training method was successfully applied in our previous research [30], the current study involved more complicated neural networks, where many more parameters of the neural network were considered. The results indicate that our training method can be successfully applied to the training of feedforward neural networks with different architectures. The training methods applied to a neural network mainly affect its convergence. The respective weaknesses of GSA and EBPA were discussed in Section 1. Here, we present the convergence performance of three training methods (GSA, EPBA, and combined GSA-EPBA) based on MRI brain data 1, as shown in Fig. 10. To observe the convergence more clearly, we examined the performance from the 7th iteration to the 200th iteration. The convergence performance of the proposed method was the best, although we can also see that the three convergence performances in the final iterations are approaching a horizontal line. Thus, we chose 200 iterations. Subsequently, we further explain why we chose the Fuzzy-RBFNN instead of RBFNN, in other words, why we chose an architecture with three hidden layers instead of one hidden layer. Whether from visual observation or objective analysis, the proposed Fuzzy-RBFNN performs better than the proposed RBFNN, even when applying the input variables of the same pattern, as shown in Figs. 5–8 (h) and (i) and Fig. 9. The principle of RBF is to cluster the variables in the input layer directly. Therefore, RBF does not analyze the characteristics of the input variables in more detail, so the reasoning conducted by RBFNN is fairly light. In contrast, by adding two hidden layers, the proposed network structure not only identifies any relationships by applying fuzzy subsets in the input space, but also provides an intuitive structure for the fuzzy reasoning rules.

To prove the statistical significance of our method, we performed 87 groups of experiments based on the entire MRI brain volume data. We adopted the 1st, 5th, 9th, …, 349th slices to interpolate the 3rd, 7th, …, 347th slices. Partial experiments are shown in Fig. 12. When compared with the performance of the curvature-based method (which performs the best overall when compared with the other three conventional methods), the images obtained by the proposed method are obviously closer to the reference images. Partial performance differences are marked by red arrows in the images. Unsurprisingly, the average MSD and ESSIM values based on the proposed method are significantly better than those of the curvature-based method, as shown in Table 3. However, owing to the extensive training required, computational time is not an advantage of the proposed method. In addition, for better evaluation of the two method, we also adopted the 1st, 3rd, 5th, 7th, …, 351th slices to interpolate the 2nd, 4th, …, 350th slices. Subsequently, for these two slice distance acquisition modes, the sensitivity analysis based on ESSIM are shown in Fig. 13. Accordingly, we can more clearly observe that the ESSIM values of the proposed method are significantly higher than those of the curvature-based method based on a whole MRI brain data.

We further discuss the selection of the ideal output data. Ideal output data plays an important role in optimizing a neural network because it is an important part of the fitness function that is directly related to the training performance of a neural network. In most research studies that applied feedforward NNs to data prediction or optimal data searching, the ideal data were normally the ground truth or perfect data [46,47]. In this study, we adopted the data obtained from the curvature-based method instead of the reference image as the ideal output data. In real cases, it is impossible to have an actual reference image available. Thus, slice interpolation must be conducted on incomplete data to obtain images that can be used in medical diagnoses. The experimental results verified that the performance of the proposed method outperforms that of the curvature-based method and other state-of-the-art methods. The results also indicate that the proposed RBFNN incorporates an effective self-learning function owing to the appropriate neural network structure and effective training method adopted.

Finally, we compared and observed the performance of the proposed neural network and convolutional neural network. As mentioned before, deep learning technology has achieved excellent results in image super-resolution. However, training convolutional neural networks requires big data. As in Ref. [20], the total number of data for training the CNN is 7670. In this study, according to Ref. [20], we also adopted U-net neural network to acquire resultant images. The difference is that the number of our training data is 300 MRI brain images from three different people, the MRI brain data from Table 1 is used as test data. Herein, 171th slice and 199th slice images are shown in Fig. 14, Compared with proposed method (The selection of input images of proposed method is also on basis of every three slices), the performances of U-net were obviously worse than that of the proposed method, whether from visual observation or from ESSIM analysis. The main reason for the poor performance of U-net neural network lies in the insufficiency of training data. This also proves that the proposed method has its own advantages compared with deep learning technology in the case of limited data. In the future study, with sufficient data, more experiments will be done to compare the convolutional neural network with the proposed neural network.

5. Conclusion

Incomplete medical imaging data interferes significantly with the diagnostic abilities. Therefore, the importance of interpolation technology is self-evident. Moreover, current interpolation algorithms have been demonstrated to have various shortcomings. In this paper, a novel method based on an EF-RBFNN was introduced to perform slice interpolation. Simultaneously, a hybrid combination of the GSA and EBPA was employed to train the proposed system. Through experiments based on four groups of real medical data, the performance of other three methods was compared to the proposed method. The results proved the validity and effectiveness of the proposed method, which outperformed the other three methods in both image observation and objective analysis.

Conflicts of interest

We declare that we do not have any commercial or associative interest that represents a conflict of interest in connection with the work submitted.

Acknowledgments

This research was supported by the Basic Science Research Program through the National Research Foundation of Korea funded by the Ministry of Science, ICT & Future Planning (NRF-2017R1A2B2001818).

References

[1] J.S. Duncan, N. Ayache, Medical image analysis: progress over two decades and the challenges ahead, IEEE Trans. Pattern Anal. Mach. Intell. 22 (1) (2000) 85–106.
[2] K. Doi, Current status and future potential of computer-aided diagnosis in medical imaging, Br. J. Radiol. 78 (suppl_1) (2005) s3–s19.
[3] S.-S. Bao, B. Lin, Research on interpolation methods for outline insert value weight arithmetic, J. Chongqing Normal Univ. (Nat. Sci. Ed.) 20 (3) (2003) 29–32.
[4] R.A. Robb, Biomedical Imaging, Visualization, and Analysis, John Wiley & Sons, Inc., 1999.
[5] J. Leng, G. Xu, Y. Zhang, Medical image interpolation based on multi-resolution registration, Comput. Math. Appl. 66 (1) (2013) 1–18.
[6] G.T. Herman, S.W. Rowland, M.-M. Yau, A comparative study of the use of linear and modified cubic spline interpolation for image reconstruction, IEEE Trans. Nucl. Sci. 26 (2) (1979) 2879–2894.
[7] T.M. Lehmann, C. Gonner, K. Spitzer, Survey, Interpolation methods in medical image processing, IEEE Trans. Med. Imaging 18 (11) (1999) 1049–1075.
[8] K.-W. Hung, W.-C. Siu, Improved image interpolation using bilateral filter for weighted least square estimation, 17th IEEE International Conference on Image Processing, ICIP), 2010.
[9] M.R. Stytz, R.W. Parrott, Using kriging for 3D medical imaging, Comput. Med. Imag. Graph. 17 (6) (1993) 421–442.
[10] C. Zhang, W. Li, D. Travis, Gaps-fill of SLC-off Landsat ETM + satellite image using a geostatistical approach, Int. J. Remote Sens. 28 (2007) 5103–5122.
[11] G. Ferrand, et al., Accelerating parallel transmit array B1 mapping in high field MRI with slice undersampling and interpolation by kriging, IEEE Trans. Med. Imaging 33 (8) (2014) 1726–1734.
[12] J.C. Carr, W.R. Fright, R.K. Beatson, Surface interpolation with radial basis functions for medical imaging, IEEE Trans. Med. Imaging 16 (1) (1997) 96–107.
[13] A. Goshtasby, D.A. Turner, L.V. Ackerman, Matching of tomographic slices for interpolation, IEEE Trans. Med. Imaging 11 (4) (1992) 507–516.
[14] G.P. Penney, et al., Registration-based interpolation, IEEE Trans. Med. Imaging 23 (7) (2004) 922–926.
[15] D.H. Frakes, et al., A new method for registration-based medical image interpolation, IEEE Trans. Med. Imaging 27 (3) (2008) 370–377.
[16] A. Baghaie, Z. Yu, Curvature-based registration for slice interpolation of medical images, International Symposium Computational Modeling of Objects Represented in Images, Springer, Cham, 2014.
[17] A. Baghaie, Z. Yu, An optimization method for slice interpolation of medical images, (2014) arXiv preprint arXiv:1402.0936.
[18] B. Fischer, J. Modersitzki, A unified approach to fast image registration and a new curvature based registration technique, Linear Algebra Appl. 380 (2004) 107–124.
[19] A. Horváth, et al., High Order Slice Interpolation for Medical Images, International Workshop on Simulation and Synthesis in Medical Imaging, Springer, Cham, 2017.
[20] Junyoung Park, et al., Computed tomography super-resolution using deep convolutional neural network, Phys. Med. Biol. 63 (14) (2018) 145011.
[21] Chenyu You, et al., CT super-resolution GAN constrained by the identical, residual, and cycle learning ensemble (GAN-CIRCLE), (2018) arXiv preprint arXiv:1808.04256.
[22] Chang Liu, et al., Fusing multi-scale information in convolution network for MR image super-resolution reconstruction, Biomed. Eng. Online 17 (1) (2018) 114.
[23] T. Takagi, M. Sugeno, Fuzzy identification of systems and its applications to modeling and control, IEEE Trans. Syst. Man. Cybern. 1 (1985) 116–132.
[24] X. Ding, et al., Parameter estimation of Takagi–Sugeno fuzzy system using heterogeneous cuckoo search algorithm, Neurocomputing 151 (2015) 1332–1342.
[25] J.R. Zhang, J. Zhang, T.M. Lock, M.R. Lyu, A hybrid particle swarm optimization back-propagation algorithm for feedforward neural network training, Appl. Math. Comput. 128 (2007) 1026–1037.
[26] E. Rashedi, H. Nezamabadi-Pour, S. Saryazdi, GSA: a gravitational search algorithm, Inf. Sci. 179 (13) (2009) 2232–2248.
[27] S. Duman, et al., Optimal power flow using gravitational search algorithm, Energy Convers. Manag. 59 (2012) 86–95.
[28] Y.M. Shuaib, M.S. Kalavathi, C.C.A. Rajan, Optimal capacitor placement in radial distribution system using gravitational search algorithm, Int. J. Elec. Power 64 (2015) 384–397.
[29] Esmat Rashedi, Elaheh Rashedi, Hossein Nezamabadi-pour, A comprehensive survey on gravitational search algorithm, Swarm Evol. Comput. 41 (2018) 141–158.
[30] S. Mirjalili, S.Z.M. Hashim, H.M. Sardroudi, Training feedforward neural networks using hybrid particle swarm optimization and gravitational search algorithm, Appl. Math. Comput. 218 (2012) 11125–11137.
[31] Aizhu Zhang, et al., A dynamic neighborhood learning-based gravitational search algorithm, IEEE Trans. Cybern. 48 (1) (2018) 436–447.
[32] Z. Chao, D. Kim, H.-J. Kim, Multi-modality image fusion based on enhanced fuzzy radial basis function neural networks, Phys. Med. 48 (2018) 11–20.
[33] B. Fischer, J. Modersitzki, A unified approach to fast image registration and a new curvature based registration technique, Linear Algebra Appl. 380 (2004) 107–124.
[34] W. Qi, et al., Stochastic stability and L1-gain analysis for positive nonlinear semi-Markov jump systems with time-varying delay via TS fuzzy model approach, Fuzzy Sets Syst. (2018), https://doi.org/10.1016/j.fss.2018.06.004.
[35] D.S. Broomhead, D. Lowe, Radial Basis Functions, Multi-Variable Functional Interpolation and Adaptive Networks, No. RSRE-MEMO-4148, Royal Signals and Radar Establishment Malvern, United Kingdom), 1988.
[36] J. Moody, C.J. Darken, Fast learning in networks of locally-tuned processing units, Neural Comput. 1 (2) (1989) 281–294.
[37] J.-S.R. Jang, C.-T. Sun, Functional equivalence between radial basis function networks and fuzzy inference systems, IEEE Trans. Neural Netw. 4 (1) (1993) 156–159.
[38] W. Xue, et al., Gradient magnitude similarity deviation: a highly efficient perceptual image quality index, IEEE Trans. Image Process. 23 (2) (2014) 684–695.
[39] M.T. Hagan, M.B. Menhaj, Training feedforward networks with the Marquardt algorithm, IEEE Trans. Neural Netw. 5 (1994) 989–993.
[40] Materialise Mimics, Materialise, http://www.materialise.com, (2017).
[41] X. Zhang, et al., Edge strength similarity for image quality assessment, IEEE Signal Process. Lett. 20 (4) (2013) 319–322.
[42] J.-J. Huang, W.-C. Siu, T.-R. Liu, Fast image interpolation via random forests, IEEE Trans. Image Process. 24 (10) (2015) 3232–3245.
[43] T. Kanade, M. Okutomi, A stereo matching algorithm with an adaptive window: theory and experiment, Proceedings of IEEE International Conference on Robotics and Automation (1991).
[44] E. Shechtman, M. Irani, Matching local self-similarities across images and videos, IEEE Conference on Computer Vision and Pattern Recognition (2007).
[45] J. Chen, et al., A simple and effective method for filling gaps in Landsat ETM + SLC-off images, Remote Sens. Environ. 115 (4) (2011) 1053–1064.
[46] X. Ding, et al., Parameter estimation of Takagi–Sugeno fuzzy system using heterogeneous cuckoo search algorithm, Neurocomputing 151 (2015) 1332–1342.
[47] S. Li, et al., Using neural networks to estimate wind turbine power generation, IEEE Trans. Energy Convers. 16 (3) (2001) 276–282.